Hydrol. Earth Syst. Sci. Discuss., 8, 529–554, 2011
www.hydrol-earth-syst-sci-discuss.net/8/529/2011/
doi:10.5194/hessd-8-529-2011


Hydrology and Earth System Sciences Discussions



# Modeling evaporation processes in a saline soil from saturation to oven dry conditions

**M. Gran[1,2], J. Carrera[1], S. Olivella[2], and M. W. Saaltink[2]**

[1]GHS, Institute of Enviromental Assessment and Water Research (IDAEA), CSIC, Barcelona, Spain
[2]Dept. Geotechnical Engineering and Geosciences, Universitat Politecnica de Catalunya, UPC-BarcelonaTech, Barcelona, Spain

Received: 16 December 2010 – Accepted: 18 December 2010 – Published: 18 January 2011

Correspondence to: M. Gran (meritxell.gran@idaea.csic.es)

Published by Copernicus Publications on behalf of the European Geosciences Union.







## Abstract

Thermal, suction and osmotic gradients interact during evaporation from a salty soil. Vapor fluxes become the main water flow mechanism under very dry conditions. A coupled nonisothermal multiphase flow and a reactive transport model of a salty sand soil was developed to study such an intricate system. The model was calibrated with data from an evaporation experiment (volumetric water content, temperature and concentration). The retention curve and relative permeability functions were modified to simulate oven dry conditions. Experimental observations were satisfactorily reproduced, which suggests that the model can be used to assess the underlying processes. Results show that evaporation is controlled by heat, and limited by salinity and liquid and vapor fluxes. Below evaporation front vapor flows downwards controlled by temperature gradient and thus generates a dilution. Vapor diffusion and dilution are strongly influenced by heat boundary conditions. Gas diffusion plays a major role in the magnitude of vapor fluxes.

## 1 Introduction

Understanding evaporation is necesary in many fields of earth system sciences (Shuttleworth, 2007). In fact, soil evaporation is crucial in controlling the balance of soil-surface water and energy in arid and semiarid areas (Saito et al., 2006). The actual mechanisms controlling evaporation are intricate (Sakai et al., 2009). Soil evaporation may be controlled by the soil-atmosphere boundary layer when the soil is moist or by hydraulic conditions when it is dry (Schneider-Zapp et al., 2010). In the latter case, evaporation causes the soil to dry and heat up causing liquid, vapor and heat fluxes to interact. The presence of solutes increases the complexity of the system and exacerbates the consequences leading to salinization.

A number of researchers have analyzed this problem from an experimental perspective (Wheeting, 1925; Scotter, 1974; Nassar and Horton, 1989; Scanlon, 1992). These





HESSD
8, 529–554, 2011



authors concluded that water flux in dry and salinized soils is controlled by salinity and temperature gradients. Salinity causes water activity to drop, thus reducing vapor pressure in equilibrium with liquid water and driving vapor towards the saltier zone. Evaporation depends also on temperature and absorbs energy. Thus, evaporation is affected by water flow and energy and solutes transport. The interaction of matric potential, temperature and salinity gradients under very dry conditions was studied by Gran et al. (2010), who observed a salinity decrease below the evaporation front owing to condensation of downward vapor flux. Although experimental studies are critical, they do not yield direct measurements of flow and phase change processes, which must be indirectly inferred from state variable measurements. This is not easy when the phenomena are complex and coupled. Therefore, quantitative understanding of the above processes requires numerical modeling.

Most models of evaporation focus on the interactions between water and heat flow (Jackson et al., 1974; Scanlon and Milly, 1994; Boulet et al., 1997). These authors conclude that vapor flux is dominant near the surface where the soil is dry, and that water flows in the liquid phase below the evaporation front. A good approximation to water table evaporation under isothermal conditions was obtained by Gowing et al. (2006), who divided the soil into liquid flow and vapor flow zones separated by the evaporation front. The nature of the evaporation front is unclear: Gran et al. (2010) observed a sharp front, whereas Konucku et al. (2004) concluded that a sharp phase transformation could not be expected. Notwithstanding, these models do not consider the role of salinity.

The effect of high salinities was modeled by Nassar and Horton (1989), who simulated water transport in unsaturated nonisothermal salty soil on the basis of steady-state heat and mass transfer. Ironically, salinity effects have commonly been predicted assuming dilute solutions, which is not sufficient to compute vapor and liquid pressures (Burns et al., 2006). This explains the difficulties encountered by Nassar et al. (1992) when modeling evaporation from salty solutions.





HESSD
8, 529–554, 2011



Two additional factors must be borne in mind when modeling evaporation from high salinity solutions. First, salt precipitates tend to form a low permeability crust that should be modeled (Yakirevich et al., 1997). Crust formation was modeled but not compared with experimental data by Olivella et al. (1996a). Second, under hot conditions, the residual saturation can no longer be considered a lower bound for saturation (Milly and Eagleson, 1982; Rossi and Nimmo, 1994; Prunty, 2003). A modification of the retention curve and relative permeability function must therefore be considered.

A nonisothermal multiphase flow model is necessary to simulate the processes under these very dry conditions. Advective and diffusive vapor flows must be allowed, and high concentration values and oven dry conditions near the surface must be acknowledged. Mass balances of water, air, heat and solutes are necessary and effects of thermal, suction and salinity gradients must be simulated interacting simultaneously.

The present work seeks to model the experiments of Gran et al. (2010) in order to (a) evaluate the magnitude and direction of the water fluxes and gain a greater understanding of the downward vapor flow mechanism, (b) describe the evolution and location of condensation-evaporation, and (c) to assess the relevance of the matric potential, temperature and osmotic gradients in controlling the aforementioned water separation process.

## 2 Evaporation experiment and conceptual model

Laboratory experiments consisted of open sand columns initially saturated with an epsomite ($MgSO_4 \cdot 7H_2O$) solution. Evaporation was forced by an infrared lamp so that radiation at the soil surface was similar to the summer radiation at mid-latitudes. The experiment continued until the overall saturation fell to 0.32. At this stage, the columns were dismounted to measure vertical profiles of temperature, volumetric water content and solute concentration. Some identical columns were dismounted at different times to obtain the time evolution of those profiles. These columns were dismantled sequentially after reaching saturation degrees of 74% (after 2 days of evaporation), 50% (after 4 days), 40% (5 days) and 32% (12 days).





HESSD
8, 529–554, 2011



Both column experiments and results are described in Gran et al. (2010) and a diagram is shown in Fig. 1.

Results displayed a coupled phenomenon. Capillarity brings about an upward liquid flux and soil drying. The liquid flux transports solutes by advection towards the top, where evaporation leads to a dramatic increase in concentration. Evaporation also reduces the water content and the unsaturated hydraulic conductivity causing the evaporation front to move downwards. Measurements suggest that this front is very narrow. A water separation process occurs at the front. On the one hand, concentrations are high above the front, where water flow is restricted to the vapor phase. On the other hand, underneath the evaporation front, concentrations are diluted below initial values. That is, vapor flows not only upwards from the evaporation front but also downwards. Condensation of this downward vapor flux causes dilution.

## 3 Processes and governing equations

The system is governed by thermohydraulic and geochemical processes. To simulate them, it is necessary to study water flow and heat and reactive transport. Changes in porosity, thermal conductivity, permeability and water activity caused by water content reduction and salt precipitation should be simulated as well as vapor pressure variations in response to changes in water activity. Moreover, the precipitates present in the system (epsomite $MgSO_4 \cdot 7H_2O$, hexahydrite $MgSO_4 \cdot 6H_2O$, pentahydrite $MgSO_4 \cdot 5H_2O$ and starkeyite $MgSO_4 \cdot 4H_2O$) are highly hygroscopic. Therefore, hydratation-dehydratation of the mineral phases must be considered in the mass water balance.

### 3.1 Thermohydraulic processes

The thermohydraulic model focuses on the mass balance of water (liquid water and vapor) and air (dissolved in water and in the gas phase) in terms of pressure, and the





HESSD
8, 529–554, 2011



energy balance in terms of temperature. The equations of water and air mass balance are:

$$\frac{\partial}{\partial t}(\omega_{\mathrm{l}}^{\mathrm{w}}\rho_{\mathrm{l}}S_{\mathrm{l}}\phi + \omega_{\mathrm{g}}^{\mathrm{w}}\rho_{\mathrm{g}}S_{\mathrm{g}}\phi) + \nabla\cdot(\boldsymbol{j}_{\mathrm{l}}^{\mathrm{w}} + \boldsymbol{j}_{\mathrm{g}}^{\mathrm{w}}) = f^{\mathrm{w}} \quad (1)$$

$$\frac{\partial}{\partial t}(\omega_{\mathrm{l}}^{\mathrm{a}}\rho_{\mathrm{l}}S_{\mathrm{l}}\phi + \omega_{\mathrm{g}}^{\mathrm{a}}\rho_{\mathrm{g}}S_{\mathrm{g}}\phi) + \nabla\cdot(\boldsymbol{j}_{\mathrm{l}}^{\mathrm{a}} + \boldsymbol{j}_{\mathrm{g}}^{\mathrm{a}}) = f^{\mathrm{a}} \quad (2)$$

where subscripts l and g refer to liquid and gas and superscript w and a refer to water and air, $\omega$ is the mass fraction ($\mathrm{kg\,kg^{-1}}$) of a component in a phase, $\rho$ is the density ($\mathrm{kg\,m^{-3}}$) of a phase, $S$ is the hydraulic saturation ($\mathrm{m^3\,m^{-3}}$), $\phi$ is the porosity ($\mathrm{m^3\,m^{-3}}$), $\boldsymbol{j}$ ($\mathrm{kg\,m^{-2}\,s^{-1}}$) is the total flux (advective, diffusive and dispersive) and $f$ is an external source/sink term ($\mathrm{kg\,m^{-3}\,s^{-1}}$).

The energy mass balance is written as:

$$\frac{\partial}{\partial t}(E_{\mathrm{s}}\rho_{\mathrm{s}}(1-\phi) + E_{\mathrm{l}}\rho_{\mathrm{l}}S_{\mathrm{l}}\phi + E_{\mathrm{g}}\rho_{\mathrm{g}}S_{\mathrm{g}}\phi) + + \nabla\cdot(\boldsymbol{i}_{\mathrm{c}} + \boldsymbol{j}_{\mathrm{El}} + \boldsymbol{j}_{\mathrm{Eg}}) = f^{Q} \quad (3)$$

where $\boldsymbol{i}_c$ is the energy flux ($\mathrm{J\,m^{-2}\,s^{-1}}$) owing to conduction through the porous medium, the other fluxes ($\boldsymbol{j}_{\mathrm{El}}, \boldsymbol{j}_{\mathrm{Eg}}$) are advective fluxes of energy ($\mathrm{J\,m^{-2}\,s^{-1}}$) caused by mass motions and $f^Q$ is an internal/external supply ($\mathrm{J\,m^{-3}\,s^{-1}}$).

A state variable is associated with each mass balance: liquid pressure ($P_{\mathrm{l}}$), gas pressure ($P_{\mathrm{g}}$) and temperature ($T$). Constitutive laws must be used to express the mass balance equations as a function of the state variables. The constitutive laws that control these balances are shown in Table 1.

### 3.2 Oven dry conditions

As discussed above, under oven-dry conditions, the residual saturation can no longer be considered a lower bound for saturation, and a modification of the retention curve and relative permeability functions must be considered. Milly and Eagleson (1982) simply considered the residual saturation to be zero; Rossi and Nimmo (1994) proposed





HESSD
8, 529–554, 2011



a different function to extend the capillary curve towards fully dry conditions; and Prunty (2003) used the zero value in standard retention curve models but modified the relative permeability function for the dry range.

The van Genuchten (1980) model is widely used under moist conditions but requires modification to represent the very dry ones. The assumption is that soil can reach full drying, i.e. if evaporation takes place in an oven at 105 °C or near the surface under a dry or hot atmosphere (Ross et al., 1991).

The van Genuchten retention curve is:

$$S_e = \left(1 + (P_c/P_0)^{\frac{1}{1-\lambda}}\right)^{-\lambda} \quad (4)$$

where $P_c$ is capillary pressure, $P_0$ is related to the capillary pressure required to desaturate the soil and $\lambda$ is a shape parameter of the function. This equation permits to calculate the effective saturation ($S_e$) as a function of a minimum saturation $S_i$ and the actual saturation ($S_l$):

$$S_e = (S_l - S_i)/(1 - S_i) \text{ or } S_l = S_i + (1 - S_i)S_e \quad (5)$$

In order to extend this curve for high suctions (i.e. conditions of drying by evaporation), the minimum degree of saturation is expressed as follows:

$$S_i = S^0_{min}\alpha \ln(P_c^{dry}/P_c) \quad (6)$$

The parameter $P_c^{dry}$ can be identified with the capillary pressure for the dry material and can be considered equal to $P_c^{\text{oven dryness}}$=1000 MPa. However, lower values may be considered if dryness is induced by atmospheric conditions that are less extreme than oven dryness. Finally, $\alpha$ modifies somewhat the transition point and $S^0_{min}$ is used in the permeability function below. This proposed retention curve is a continuous function with continuous derivatives. A similar form was already proposed by Fayer and Simmons (1995).





HESSD
8, 529–554, 2011



The following relative permeability function is proposed for the new retention curve

$$K_{rl} = 0, \quad S_l \le S^0_{min}$$
$$K_{rl} = \sqrt{S_{ep}}\left(1-\left(1-S_{ep}^{1/\lambda}\right)^{\lambda}\right)^2, \quad S_l > S^0_{min} \tag{7}$$
$$S_{ep} = (S_l - S^0_{min})/(1-S^0_{min})$$

Note that for saturations below $S^0_{min}$ the capillary pressure can be calculated from the retention curve, but the relative permeability is zero. This allows representing water isolated in the meniscus that can not flow as a liquid phase but can still evaporate. Figure 2 compares the proposed model and the original van Genuchten model, in terms of retention curve and relative permeability. The parameters used here (see Table 1) are obtained by calibration. Based on these results, the incorporation of a branch for the drying process of the residual water of the soil becomes necessary.

### 3.3 Reactive transport

The mass balance used for the reactive transport can be written as

$$\frac{\partial \phi S_l \rho_l \boldsymbol{c}_a}{\partial t} = L_l(\boldsymbol{c}_a) + R \tag{8}$$
$$L_l() = -\nabla\cdot(\boldsymbol{q}_l\rho_l()) + \nabla\cdot(\boldsymbol{D}_l\phi S_l\rho_l\nabla()) + m_l$$
$$R = r_{eps} + r_{hex} + r_{pent} + r_{stark}$$
$$r_{min} = \sigma_{min}k(\Omega_{min}-1)$$

where vector $\boldsymbol{c}_a$ (mol/kg) is the concentration of aqueous species and $L_l$ is the linear operator for the advection, dispersion/diffusion, $m_l$ is the non-chemical source-sink (mol m$^{-3}$ s$^{-1}$) and $\boldsymbol{D}_l$ is the dispersion/diffusion tensor (m$^2$ s$^{-1}$). $R$ contains the rates of the kinetic reactions ($r_{min}$) for all the different mineral phases ($r_{eps}$, $r_{hex}$, $r_{pent}$ and $r_{stark}$), $\sigma_{min}$ is the mineral reactive surface and $\Omega_{min}$ is the ratio between the ion activity product and the equilibrium constant. The reaction rates enable us to estimate the liquid





HESSD
8, 529–554, 2011



water provided by mineral hydratation-dehydratation. This amount of water is added to the water mass balance as a source/sink term ($f_l^w$) in Eq. 1.

$$f_l^w = (7r_{eps} + 6r_{hex} + 5r_{pent} + 4r_{stark})m_w \quad (9)$$

where $m_w$ is the water molecular weight.

## 4 Numerical model

The problem is considered one dimensional in a vertical direction. The grid is made up of 240 elements (for 24 cm column length) consisting of two materials: the first covers the top 1.5 cm, and the second the rest. The gas diffusion enhancement factor ($\tau_0$) (see Table 1) was calibrated to be 1.2 in the upper material and 8 below. Accordingly, we reduce the vapor diffusion near the column surface, simulating more salt precipitates (salt crust formation), thereby reproducing more accurately the experimental results.

Different boundary conditions (BC) for liquid, vapor and heat were chosen to reproduce the laboratory conditions (see Table 2). The top boundary is a mixed condition representing gas (air and vapor) and heat inflow-outflows. A radiative heat flux (from the lamp) was added at the top boundary condition. The lateral and bottom BC were of no-flow for water and solutes, but some loss of energy was permitted to dissipate across the boundary.

Initial conditions are also applied: initial porosity ($\phi$=0.4), initial gas and liquid pressures ($P_g$=$P_l$=0.101325 MPa) and initial temperature ($T_0$=25 °C).

Numerical simulations were carried out using the RETRASO-CODE_BRIGHT (RCB) code, which couples the thermohydraulic model CODE_BRIGHT (CB) of Olivella et al. (1996b) with the reactive transport model RETRASO of Saaltink et al. (2004). Furthermore, geochemical calculations are performed with the object-oriented chemical module CHEPROO (Bea et al., 2009, 2010), which includes high salinity solutions using the equations of Pitzer (1973). The feedback of reactive transport in thermohydraulics is performed by a time lag approach. The code solves the thermohydraulic equations





HESSD
8, 529–554, 2011



(Eqs. 1–3) for one time step. Results (Darcy fluxes, hydraulic saturation, etc.) are used to calculate the reactive transport for the same time step (Eq. 8). Subsequently, thermohydraulic properties such as porosity change due to precipitation-dissolution or water activity and the source/sink term ($f_l^w$) are calculated using the reactive transport results. A new thermohydraulic time step is calculated using these new properties.

## 5 Results and discussion

Figure 3 displays the water saturation, temperature and salinity profiles computed for four different times along with the experimental results at the end of the experiment, after 12 days. Saturation profiles illustrate the progressive desaturation of the columns from the top. The water content drops over time to values near residual saturation at a depth that increases with time. Saturation at the top reaches oven dry conditions (volumetric water content lower than the residual one). The bottom of this zone represents the location of the evaporation front. Below it, the water content continues to increase downwards, leading to a degree of saturation profile similar to that of the sand retention curve. The good match between model and experiment at the upper oven dry area (above 4 cm depth) confirms the validity of the retention curve modification, which improves the simulation of multiphase flow under very dry conditions.

Temperature rises during the experiment and displays a slope change at the evaporation front. The temperature gradient is larger above than below the front because the evaporation front acts as a heat sink. Another smaller temperature slope change can be detected at a depth of 1.5 cm. This is due to the change in enhancement factor ($\tau_0$).

The spatial distribution of concentration is noteworthy. Salinity is extremely high at the surface, where the water content is negligible, reaching salt solubility and producing precipitates. This high concentration zone grows with time, advancing in depth with the evaporation front. Immediately below, salinity drops sharply to values underneath the initial concentration. The minimum concentration is always located immediately below the evaporation front. Further down, salinity rises slightly with depth, but still more





HESSD
8, 529–554, 2011



dilute than the initial conditions. The water content and temperature profiles coincide with what might be expected (drier and warmer conditions at the surface than at depth) unlike the concentration profile. Furthermore, a difference between the experimental data and the numerical model is observed: the minimum in the simulated concentration consistently beneath the measured one.

The fact that the model reproduces qualitatively the observations suggests that it can be used to determine the role of water flow, heat and transport processes in the system. We discuss below the mechanism that is responsible for the dilution of the solution.

Figure 4 displays the profiles of water and heat fluxes for the same instants as in Fig. 3. Liquid water flows upwards because of capillarity throughout the experiment. An evaporation front, located where the liquid flux drops abruptly to zero, may be observed after 3.3 days. This front advances deeper into the soil as the feeding liquid flux from the bottom diminishes over time. Above this front, water can no longer flow as a liquid. Nevertheless the water content continues to diminish towards the top of the column in response to the upward increase in temperature and the reduction of vapor pressure (which causes an upward decrease in relative humidity). Water vapor flux profiles show that vapor flows both upwards and downwards from the evaporation front. The increase in suction at the surface leads to a lower vapor pressure that promotes the upward flux. The temperature gradient causes a vapor pressure gradient that generates the downward flux. Condensation of this downward vapor flux accounts for the decrease at the bottom of the column and for the dilution of the solution below the evaporation front. Both upward and downward vapor fluxes are present all over the experiment.

The numerical model also enables us to study in detail heat fluxes. Figure 4 displays that conductive heat flows downwards throughout the column. This flux is larger in the upper zone, where the soil is dry, and decreases over time. Note the sudden fall in heat flux observed at all time steps, which is due to the heat sink produced by evaporation. The advance of the evaporation front is observed very clearly and its location is controlled by the above heat flux, which decreases because of depth and





HESSD
8, 529–554, 2011



dryness. The total heat flux graph exposes that conductive and advective heat fluxes are similar in magnitude but in opposite directions above the front. Below it, both fluxes flow downward although the advective flux is the dominant one.

Figure 5 displays the spatial distribution of the evaporation and condensation rates and the vapor mass fraction profile. The vapor mass fraction profile presents a marked change in the slope and provides evidence of two distinct gradients. Since evaporation occurs at this juncture, the increase in vapor and gas pressure generates vapor diffusion and advection both upwards and downwards. The graph on the right displays the evolution of the evaporation (negative values). The evaporation rate is higher at the start and decreases as the evaporation front advances deeper into the soil. Condensation rate is much smaller than evaporation, but extends over a much longer interval. Vapor condensation occurs from the early stages and its maximum evolves decreasing and advancing into the soil just like evaporation. This explains the decrease in concentration below its initial value. Nevertheless, the model underestimates this decrease. Note that condensation always occurs below the evaporation front and that its magnitude is substantially lower than that of the evaporation, causing the soil to dry.

## 6 Sensitivity analisis

Further insight into the above processes and into the role of controlling parameters can be gained from a sensitivity analysis. Processes are strongly coupled, i.e. all the parameters affect all the processes. We focused on the sensitivity of the boundary heat dissipation ($\gamma$) and the gas diffusion enhancement factor ($\tau_0$), which proved to be more illustrative. Table 3 presents the values adopted for these parameters.

Figure 6 illustrates the impact of the heat dissipation increase through the column walls on the whole system. The effect of the heat dissipation increase through the bottom has also been studied but is not shown here (it presents a similar system response but less relevant). Increasing $\gamma$ at the walls causes an increase in the rate of sensible heat dissipation and leaves less energy available for evaporation. Although





HESSD
8, 529–554, 2011



Fig. 6 shows higher evaporation at the evaporation front, this is overcompensated by a higher condensation below the front. As a result the overall saturation increases and the evaporation front remains close to the surface. It also leads to a lower overall temperature. Note that as more heat is dissipated the temperature gradient just beneath the evaporation front also increases. This causes an increase in the downwards vapor pressure gradient and in the downward vapor flux, whereas, the upward vapor flux diminishes. The shape of the condensation profile varies to give a bigger maximum concentrated just below the evaporation front. We can infer that the amount of heat dissipated through the walls controls the thermal gradient in the column.

The gas diffusion enhancement factor ($\tau_0$) was homogenised increasing its value in the upper part of the column (Table 3). As a result, the soil dries faster and the overall degree of saturation diminishes. The evaporation front advances deeper into the soil and the area below is colder. The temperature profile changes from three to two different gradients: the temperature gradient near the surface increases and becomes uniform towards the evaporation front. As the lower temperature leads to less lateral heat dissipation, the temperature gradient below the evaporation front decreases. Accordingly, the downward vapor flux diminishes and hence, the condensation. By contrast, the upward vapor flux increases, showing that vapor can flow more easily towards the surface and explaining the downward displacement of the evaporation front and the column drying. As the evaporation front advances deeper into the soil, condensation takes place further down. Overall, the results fit to experimental data, suggesting that variations in $\tau_0$ must be modeled.

## 7 Conclusions

The model reproduces quite accurately experimental observations, so that it can be used to quantify processes. These confirm the initial conjecture about the highly coupled and rather complex nature of evaporation from a soil. In essence, evaporation is driven by heat, but it can be limited by liquid and vapor flux processes and by salinity.





HESSD
8, 529–554, 2011



Some conclusions can be inferred from the calibrated model:

- Evaporation causes vapor pressure to increase at the evaporation front causing vapor to flow upwards and downwards. Both fluxes occur throughout the experiment, but the relative importance of the downwards flux increases over time. In our model the downward flux is half that of the upward flux at the end of the experiment.

- The evaporation front is very narrow, which contradicts the analysis of Konucku et al. (2004). Most evaporation is concentrated in less than 1 cm. Some evaporation occurs above the front, but condensation starts immediately below. This finding may be due to the experimental conditions (loss of heat through the column walls). Without this heat loss, water vapor could have penetrated further into the soil, which is consistent with the findings of Scanlon and Milly (1994).

- Condensation of the downward vapor flux dilutes the solution beneath the evaporation front with the result that salinity drops below the initial value. This finding confirms the existence of a water separation process driven by evaporation.

- Heat flows downwards from the surface to the bottom of the column mainly by conduction. Even though is not shown in the graphs, the advective vapor heat flux is larger than the liquid one during all the experiment. Advection of latent heat is the main transport mechanism in the system.

Further conclusions can be drawn from the sensitivity analysis:

- Vapor diffusion is very sensitive to the heat boundary conditions. The amount of heat dissipated throughout the column walls controls the temperature gradient. Downward diffusion is enhanced by the lateral heat dissipation through the walls.

- It is the temperature gradient more than the temperature range, what governs the magnitude of vapor fluxes. Therefore, these processes can occur in salinized soils under temperatures lower than the ones observed here.





HESSD
8, 529–554, 2011



- The formation of a crust due to salt precipitation reduces porosity and increases tortuosity, which hinders evaporation. These have been simulated by reducing the gas diffusion enhancement factor ($\tau_0$) at the crust. This has been needed to reproduce evaporation rates together with observed temperatures and salinity profiles.

Finally, further research is warranted to resolve a number of issues. The dilution simulated by the numerical model is always lower than that measured in the experiments. The representation of vapor flux may not be accurate. In fact, as stated by Shokri et al. (2009), the use of gas diffusion enhancement factor is an empirical need without a firm foundation. Nevertheless, our model offers new insights into the evaporation and water separation processes that occur in a salty soil under very dry conditions.

*Acknowledgements.* We gratefully acknowledge the financial support received from the EU WATCH project (WATer and global Change) and the Spanish Research Council ATRAPO project.

## References

Bea, S. A., Carrera, J., Ayora, C., Batlle, F., and Saaltink, M. W.: CHEPROO: A Fortran 90 object-oriented module to solve chemical processes in Earth science models, Comput. Geosci., 35, 1098–1112, 2009. 537

Bea, S. A., Carrera, J., Ayora, C., and Batlle, F.: Modeling of concentrated aqueous solutions: efficient implementation of Pitzer equations in geochemical and reactive transport models, Comput. Geosci., 36, 526–538, doi:10.1016/j.cageo.2009.09.004, 2010. 537

Boulet, G., Braud, I., and Vauclin, M.: Study of the mechanisms of evaporation under arid conditions using a detailed model of the soil-atmosphere continuum. Application to the EFEDA I experiment, J. Hydrol., 193, 114–141, 1997. 531

Burns, E. R., Selker, J. S., Parlange, J. Y., and Guenther, R. B.: Effects of sodium chloride on constitutive relations in variably saturated porous media, Water Resourc. Res., 42, W05405, doi:10.1029/2005WR004060, 2006. 531





HESSD

8, 529–554, 2011



Fayer, M. J. and Simmons, C. S.: Modified soil-water retention functions for all matric suctions, Water Resourc. Res., 31, 1233–1238, 1995. 535
Gowing, J. W., Konukcu, F., and Rose, D. A.: Evaporative flux from a shallow watertable: the influence of a vapour-liquid phase transition, J. Hydrol., 321, 77–89, 2006. 531
Gran, M., Carrera, J., Massana, J., W. Saaltink, M., Olivella, S., Ayora, C., and Lloret, A.: Dynamics of water vapor flux and water separation processes during evaporation from a salty dry soil, J. Hydrol., 396, 215–220, doi:10.1016/j.jhydrol.2010.11.011, 2011. 531, 532, 533
Jackson, R. D., Reginato, R. J., Kimball, B. A., and Nakayama, F. S.: Diurnal soil-water evaporation – comparison of measured and calculated soil-water fluxes, Soil Sci. Soc. Am. J., 38, 861–866, 1974. 531
Konucku, F., Istanbulluoglu, A., and Kocaman, I.: Determination of water content in drying soils: incorporating transition from liquid phase to vapour phase, Aust. J. Soil Res., 42, 1–8, 2004. 531, 542
Milly, P. and Eagleson, P.: Parameterization of moisture and heat fluxes across the land surface for use in atmospheric general circulation models, Tech. Rep. 279, R. M. Parsons Laboratory, Dept. of Civil Eng., Massachusetts Institute of Technology, Cambridge, 1982. 532, 534
Nassar, I. N. and Horton, R.: Water transport in unsaturated non-isothermal salty soil. 2. Theoretical development, Soil Sci. Soc. Am. J., 53, 1330–1337, 1989. 530, 531
Nassar, I. N., Horton, R., and Globus, A. M.: Simultaneous transfer of heat, water, and solute in porous-media. 2. Experiment and analysis, Soil Sci. Soc. Am. J., 56, 1357–1365, 1992. 531
Olivella, S., Carrera, J., Gens, A., and Alonso, E. E.: Porosity variations in saline media caused by temperature gradients coupled to multiphase flow and dissolution/precipitation, Transp. Porous Media, 25, 1–25, 1996a. 532
Olivella, S., Gens, A., Carrera, J., and Alonso, E. E.: Numerical formulation for a simulator (CODE_BRIGHT) for the coupled analysis of saline media, Engin. Comput., 13, 87–112, 1996b. 537
Pitzer, K. S.: Thermodynamics of electrolytes. 1. Theoretical basis and general equations, J. Phys. Chem., 77, 268–277, 1973. 537
Prunty, L.: Soil water retention and conductivity when vapor flow is important, J. Irrig. Drain. Eng.-ASCE, 129, 201–207, 2003. 532, 535
Ross, P. J., Williams, J., and Bristow, K. L.: Equation for extending water-retention curves to dryness, Soil Sci. Soc. Am. J., 55, 923–927, 1991. 535





HESSD
8, 529–554, 2011



Rossi, C. and Nimmo, J. R.: Modeling of soil-water retention from saturation to oven dryness, Water Resour. Res., 30, 701–708, 1994. 532, 534
Saaltink, M. W., Batlle, F., Ayora, C., Carrera, J., and Olivella, S.: RETRASO, a code for modeling reactive transport in saturated and unsaturated porous media, Geol. Acta, 2(3), 235–251, 2004. 537
Saito, H., Simunek, J., and Mohanty, B. P.: Numerical analysis of coupled water, vapor, and heat transport in the vadose zone, Vadose Zone J., 5, 784–800, 2006. 530
Sakai, M., Toride, N., and Simunek, J.: Water and vapor movement with condensation and evaporation in a sandy column, Soil Sci. Soc. Am. J., 73, 707–717, 2009. 530
Scanlon, B. R.: Evaluation of liquid and vapor water-flow in desert soils based on Cl-36 and tritium tracers and nonisothermal flow simulations, Water Resour. Res., 28, 285–297, 1992. 530
Scanlon, B. R. and Milly, P. C. D.: Water and heat fluxes in desert soils. 2. Numerical simulations, Water Resour. Res., 30, 721–733, 1994. 531, 542
Schneider-Zapp, K., Ippisch, O., and Roth, K.: Numerical study of the evaporation process and parameter estimation analysis of an evaporation experiment, Hydrol. Earth Syst. Sci., 14, 765–781, doi:10.5194/hess-14-765-2010, 2010. 530
Scotter, D. R.: Salt and water movement in relatively dry soil, Aust. J. Soil Res., 12, 27–35, 1974. 530
Shokri, N., Lehmann, P., and Or, D.: Critical evaluation of enhancement factors for vapor transport through unsaturated porous media, Water Resourc. Res., 45, W10433, doi:10.1029/2009WR007769, 2009. 543
Shuttleworth, W. J.: Putting the “vap” into evaporation, Hydrol. Earth Syst. Sci., 11, 210–244, doi:10.5194/hess-11-210-2007, 2007. 530
van Genuchten, M.: A closed-form equation for predicting the hydraulic conductivity of unsaturated soils, Soil Sci. Soc. Am. J., 44, 892–898, 1980. 535
Wheeting, L. C.: Certain relationships between added salts and the moisture of soils, Soil Sci., 19, 287–299, 1925. 530
Yakirevich, A., Berliner, P., and Sorek, S.: A model for numerical simulating of evaporation from bare saline soil, Water Resour. Res., 33, 1021–1033, 1997. 532





HESSD
8, 529–554, 2011



**Table 1.** Constitutive laws, parameters and values used in the numerical model.

| Constitutive laws | | Parameters and values |
|---|---|---|
| Water saturation for | $S_l = S_i + (1-S_i)S_e$ | $S^0_{min}=0.08$, $\alpha=0.1$ |
| ret. curve in modified | $S_e = \left(1+(P_c/P_0)^{\frac{1}{1-\lambda}}\right)^{-\lambda}$ | $\lambda=0.93$, $P_0=0.0025$ MPa |
| van Genuchten model | $S_i = S^0_{min}\alpha \ln\left(P_c^{dry}/P_c\right)$ | $P_c^{dry}=650$ MPa |
| Relative permeability function | $K_{rl} = \sqrt{S_{ep}}\left(1-\left(1-S_{ep}^{1/\lambda}\right)^{\lambda}\right)^2$ | $\lambda=0.93$ |
| (for a new ret. curve) | $S_{ep} = \left(S_l - S^0_{min}\right)/\left(1-S^0_{min}\right)$ | |
| Intrinsic permeability for | $q_\alpha = -\frac{k k_{r\alpha}}{\mu_\alpha}(\nabla P_\alpha - \rho_\alpha g)$ | $k_0 = 2.8\times10^{-11}$ m$^2$ |
| Darcy's Law | $k = k_0 \exp(b(\phi-\phi_0))$ | $b=40$, $\phi_0=0.4$ |
| Diffusive flux of vapor | $i_\alpha = -(\tau\phi\rho_\alpha S_\alpha D_m \boldsymbol{I})\nabla w_\alpha$ | $D = 5.9\times10^{-6}$ m$^2$ s$^{-1}$ K$^{-n}$ Pa |
| (Fick's Law) | $D_m = \tau D\left(\frac{(273.15+T)^n}{P_g}\right)$ | $n=2.3$ |
| | $\tau = \tau_0\left(S_g^m\right)$ | $\tau_0=8$, $m=3$ |
| Conductive flux of heat | $\lambda_{dry} = (1-\phi)^n\lambda_{solid} + \phi^n\lambda_{gas}$ | $\lambda_{sol} = 2$ W mK$^{-1}$, $n=2$ |
| (Fourier's Law) | $\lambda_{sat} = (1-\phi)^n\lambda_{solid} + \phi^n\lambda_{liq}$ | $\lambda_{gas} = 0.01$ W mK$^{-1}$ |
| | $\lambda = \sqrt{S_l}\lambda_{sat} + \left(1-\sqrt{S_l}\right)\lambda_{dry}$ | $\lambda_{liq} = 0.6$ W mK$^{-1}$ |
| Psychrometric Law | $P_v = 136075 a_w \exp\left(\frac{-5239.7}{273.15+T}\right)$ | MPa |

Where $a_w$ is the molar mass fraction of water in liquid calculated by the reactive transport from aqueous concentrations.





HESSD
8, 529–554, 2011



**Table 2.** Liquid, vapor and heat boundary conditions and corresponding parameters.

| Boundary conditions | Top | Lateral | Bottom |
|---|---|---|---|
| Liquid flux | $j_l=0$ | $j_l=0$ | $j_l=0$ |
| Vapor flux | $(\omega_g^w)^0=0.020\,kg/kg$ | | |
| $j_g^w=(\omega_g^w)^0 j_g^0+$ | $(P_g)^0=0.101325\,MPa$ | | |
| $+(\omega_g^w)^0\gamma_g(P_g^0-P_g)+$ | $\gamma_g=50\,kg/s/MPa/m^2$ | | |
| $+\beta_g((\rho_g\omega_g^w)^0-(\rho_g\omega_g^w))$ | $\beta_g=0.03\,m/s$ | | |
| | $\rho_g=1.12\,kg/m^3$ | | |
| Energy flux | $j_e^0=750\,J/s$ | $j_e^0=0$ | $j_e^0=0$ |
| $j_e=j_e^0+\gamma_e(T^0-T)+E_g^w(j_g^w)$ | $T^0=25\,^\circ C$ | $T^0=26\,^\circ C$ | $T^0=26\,^\circ C$ |
| | $\gamma_e=24\,J/s/C/m^2$ | $\gamma_e=25\,J/s/C/m^2$ | $\gamma_e=1\,J/s/C/m^2$ |





HESSD
8, 529–554, 2011



**Table 3.** Studied parameters for the sensitivity analysis: boundary heat dissipation (at the walls and at the bottom) and gas diffusion enhancement factor ($\tau_0$). Compared to the base model (BM): the boundary heat dissipation, by means of $\gamma$ value, has been doubled and increased by an order of magnitude alternatively and $\tau_0$ value for the upper material (firsts 1.5 cm) has been increased from 1.2 to 8 to equal the value for all the column.

| | Model | | | | | |
|---|---|---|---|---|---|---|
| Parameter | BM | $2\gamma_{bot}$ | $10\gamma_{bot}$ | $2\gamma_{wall}$ | $10\gamma_{wall}$ | $\tau_0$ |
| $\gamma_{wall}$ | **1** | 1 | 1 | **2** | **10** | 1 |
| $\gamma_{bottom}$ | **25** | **50** | **250** | 25 | 25 | 25 |
| $\tau_0$ | **1.2** | 1.2 | 1.2 | 1.2 | 1.2 | **8** |





HESSD
8, 529–554, 2011



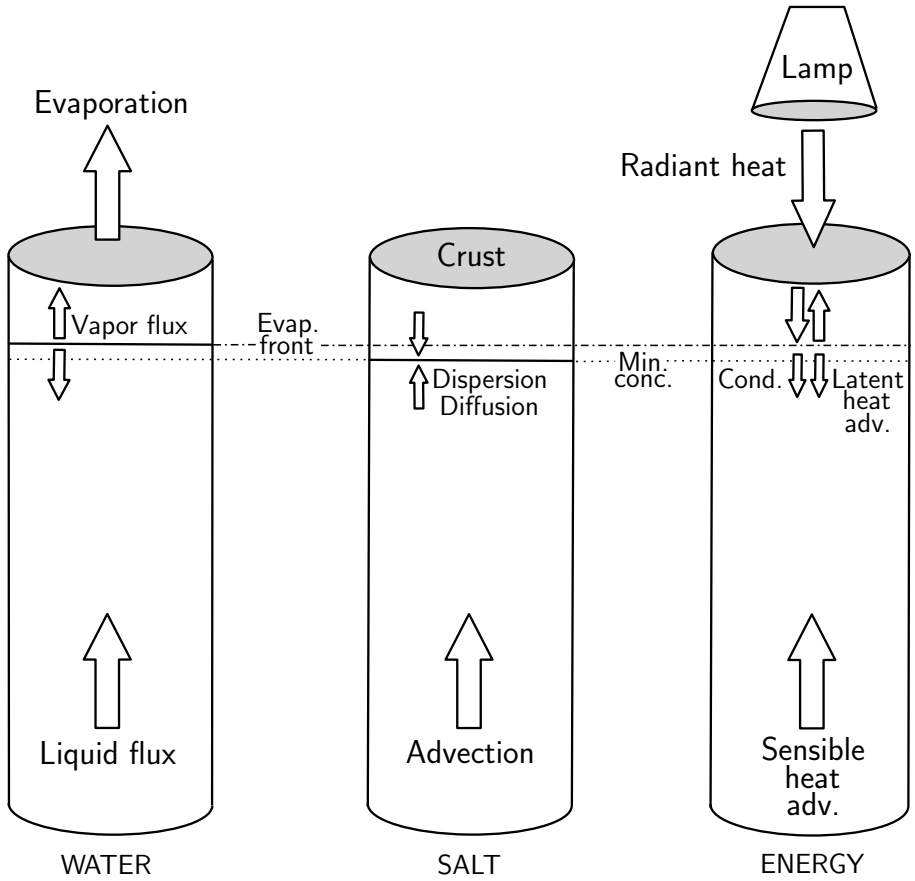


**Fig. 1.** Diagram of the design of the evaporation column experiments and their conceptual model. The water fluxes are on the left, the salt fluxes are on the centre and the energy ones on the right.





HESSD
8, 529–554, 2011



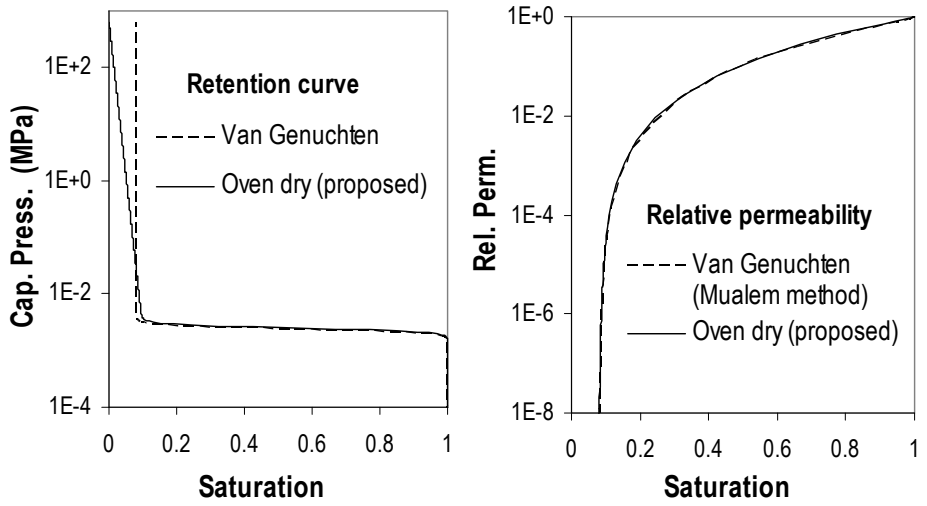


**Fig. 2.** Retention and relative permeability curves (original van Genuchten and oven dry proposed models) for the sand used in the column experiments.





HESSD
8, 529–554, 2011



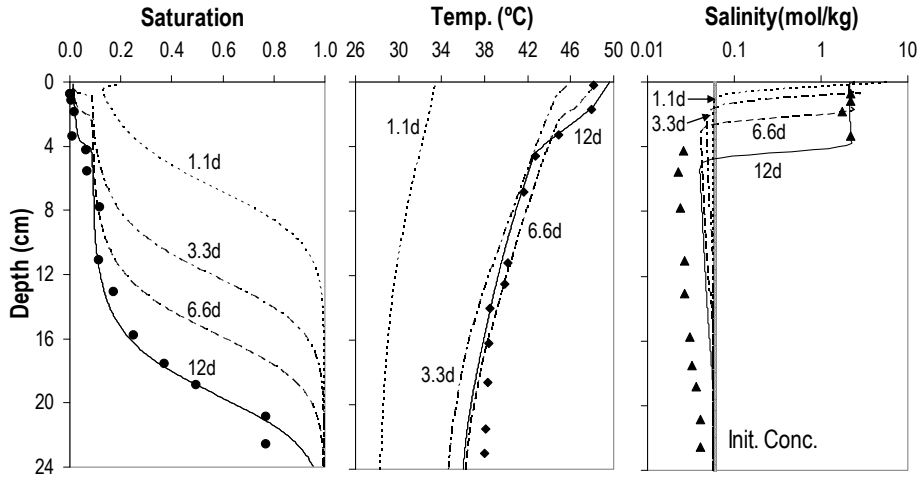


**Fig. 3.** Profiles of saturation, temperature and salinity measured at the end of the experiment (symbols) and computed (lines). The time evolution is shown for four different times (after 1.1 days, 3.3 days, 6.6 days and, at the end of the experiment, 12 days).





HESSD
8, 529–554, 2011



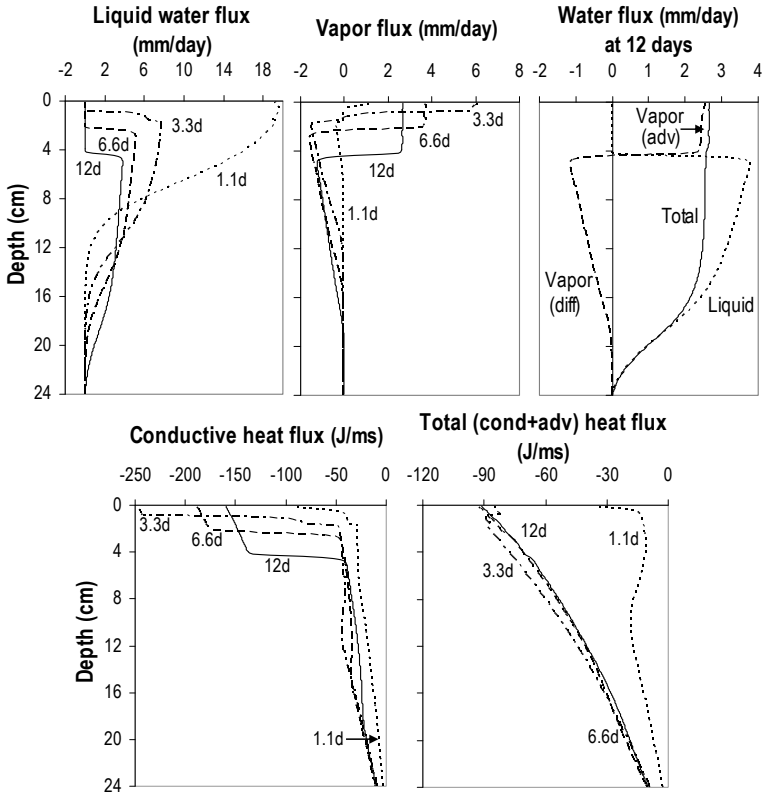


**Fig. 4.** Computed profiles of liquid, vapor and total water fluxes (above), and conductive and total (conductive plus advective) heat fluxes (below). Positive and negative values stand for upward and downward flows, respectively. The simulation results are shown for four different times (after 1.1 days, 3.3 days, 6.6 days and 12 days). The difference between the diffusive vapor flux and the total water flux, displayed in the top 4 cm of the above graph on the right, is equal to the advective vapor flux.





HESSD
8, 529–554, 2011



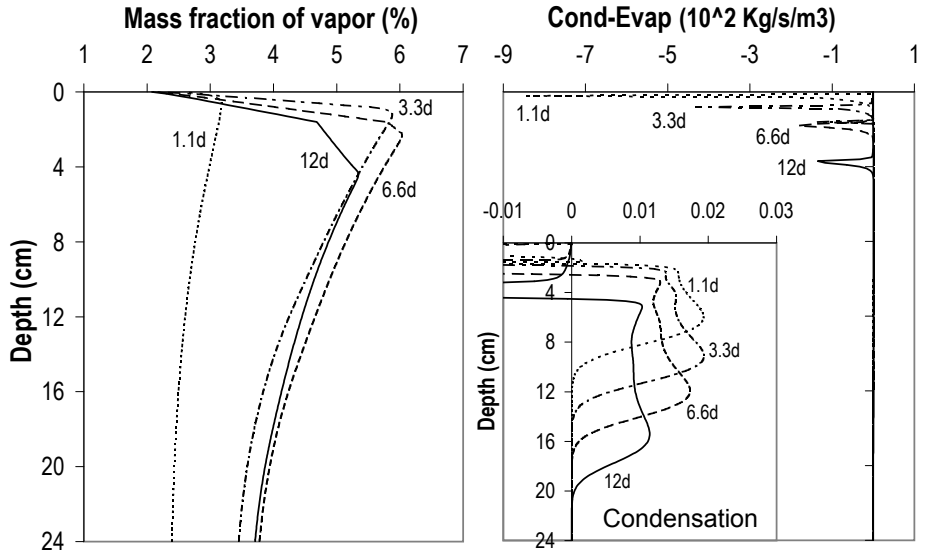


**Fig. 5.** Computed profiles of vapor mass fraction and evaporation (negative)/condensation (positive) rates for four different times. Note the change in the vapor mass fraction slope at 1.5 cm depth owing to the imposition of the reduction in vapor diffusivity on the salt crust.





HESSD
8, 529–554, 2011



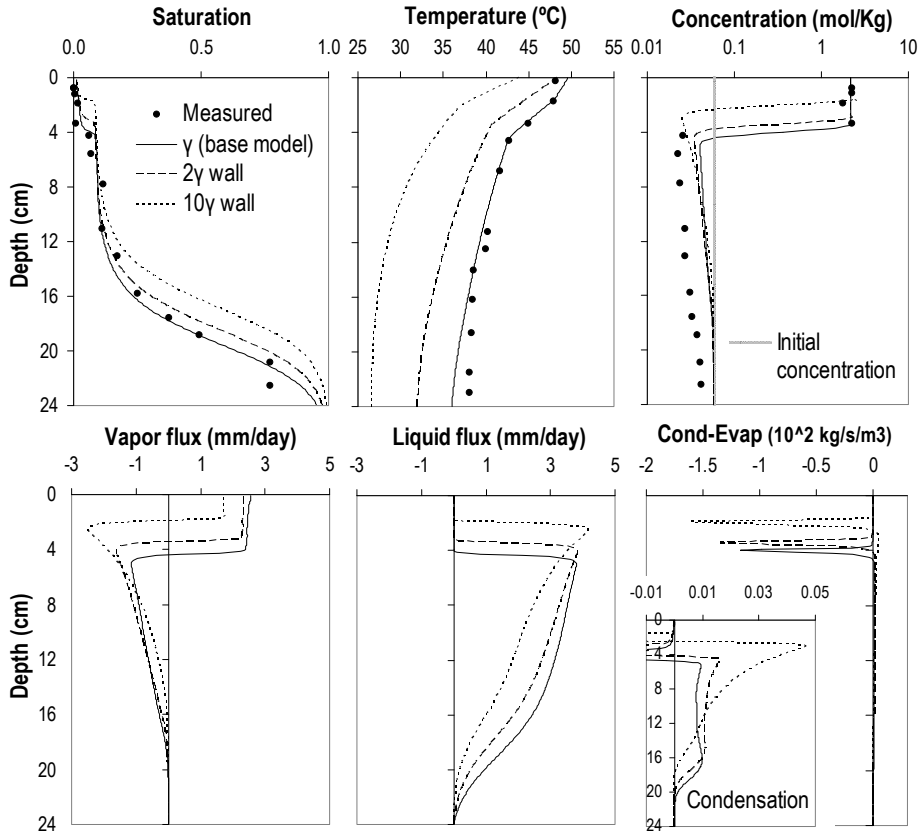


**Fig. 6.** Analysis of the effect of boundary heat dissipation. Computed profiles of saturation, temperature, concentration, water mass flux, evaporation and condensation after 12 days.





HESSD
8, 529–554, 2011